Illuminating the photomechanical effect: Exploring the relationship between electron-hole excitation and deformation mechanisms in nanotwinned boron carbide

Yi He,[1] Yidi Shen,[2] Bin Tang,[1,*] and Qi An[2,†]

[1]*State Key Laboratory of Electronic Thin Films and Integrated Devices, University of Electronic Science and Technology of China, Chengdu, 610054, China*

[2]*Department of Materials Science and Engineering, Iowa State University, Ames, Iowa 50011, USA*

(Received 23 April 2023; accepted 24 May 2023; published 6 June 2023)

The photomechanical effect, a phenomenon in which electron-hole (e-h) excitation from light illumination influences the plastic deformation of semiconductors, remains poorly understood at the microscopic level. In this study, we employ constrained density-functional theory simulations to investigate the interaction between e-h excitation and twin boundaries in nanotwinned boron carbide (B_4C) and their impact on deformation mechanisms. Our findings reveal that excited e-h pairs reduce both the critical displacement (or critical shear strain) and shear strength of nanotwinned B_4C under shear-induced failure. This reduction stems from the redistribution of electrons and holes near the twin boundary, weakening the B–C bond connecting adjacent icosahedra and leading to cage destabilization and failure. Notably, e-h excitation alters the deformation mechanism of asymmetric twins while exacerbating that of symmetric twins. These simulation results offer a physical explanation for the observed softening effects in nanotwinned materials under e-h excitation, thereby contributing to the understanding of the photomechanical effect.

DOI: 10.1103/PhysRevB.107.224102

I. INTRODUCTION

Twin boundaries (TBs) frequently form during crystal growth, annealing, and deformation processes [1,2]. These boundaries separate two crystals along a mirror plane, with TBs exhibiting smaller lattice mismatches resulting in lower interfacial energy compared to conventional incoherent grain boundaries (GBs) [3]. Consequently, the incorporation of TBs in real-world materials significantly affects their mechanical, electronic, and thermal transport properties [4–6]. The formation of nanoscale twins, in particular, holds considerable potential for influencing the strength and plasticity of ceramics and metals [7–9]. For instance, nanotwinned copper samples exhibit a tenfold increase in strength compared to coarse-grained copper [5]. Additionally, recent experimental studies have reported substantially enhanced hardness and strength in nanotwinned boron nitride [10,11] and nanotwinned diamond [12].

Numerous studies [13–19] have documented the presence of a significant number of growth twins in sintered boron carbide (B_4C). Owing to its exceptional properties such as ultrahigh hardness, low density, and excellent thermal stability, B_4C is a superhard material extensively employed in various engineering applications [20–22]. The mechanical properties of boron carbide, similar to other ceramics and metal alloys, are often associated with its chemical composition, fabrication processes, and microstructures. B_4C features a complex crystalline structure consisting of a C-B-C chain and a $B_{11}C$ icosahedron within a rhombohedral unit cell. Density-functional theory (DFT) simulations [23] indicate that the energetically favorable structure is $(B_{11}C_p)$CBC, with one carbon atom situated in the cage and connected to the adjacent icosahedron (denoted by subscript p for polar site). The $(B_{11}C_e)$CBC structure, wherein the equatorial carbon atom in the cage links to the C-B-C chain (denoted by subscript e for equatorial site), is less stable.

Fujita *et al.* [15] identified and characterized novel planar defects in boron carbide using spherical aberration-corrected scanning transmission electron microscopy. Although these planar defects initially appeared as conventional twin boundaries, further analysis revealed that the lattices did not exhibit exact mirror symmetry, with the angles between the (100) and (010) planes differing by approximately 2° on either side of the TBs [15]. Due to the lack of mirror symmetry, these new planar defects were termed "asymmetric twins" [15]. Subsequently, Xie *et al.* [16] integrated *ab initio* simulations and transmission electron microscopy (TEM) observations to determine that asymmetric twins were, in fact, phase boundaries of $(B_{11}C_p)$CBC and $(B_{11}C_e)$CBC.

A substantial body of research highlights the significance of nanotwins in determining the thermal and mechanical properties of icosahedral superhard materials [8,13,24,25]. For instance, nanoindentation experiments and DFT simulations have shown that nanotwins in B_4C (including both asymmetric and symmetric twins) contribute to increased strength relative to perfect crystals [13]. The directional nature of covalent bonds inhibits slipping along the twin boundary, resulting in a strengthening mechanism. Conversely, nanotwins in boron-rich boron carbide ($B_{13}C_2$) reduce strength due to interactions between the TB and the C-B-C chains that connect the B_{12} icosahedra [24]. Additionally, theoretical studies [8] have reported a 7.5% decrease in the ideal

*tangbin@uestc.edu.cn
†qan@iastate.edu

shear strength of nanotwinned B_6O compared to the perfect structure. Furthermore, a recent DFT investigation has demonstrated that nanotwinned r-$LiB_{13}C_2$ not only exhibits enhanced strength compared to r-$LiB_{13}C_2$ but also surpasses the strength of B_4C [26]. With respect to thermal transport, Huang *et al.* [27] found that TBs substantially impede phonon transport in all directions within nanotwinned $B_{12}P_2$, leading to low thermal conductivity.

B_4C is a *p*-type semiconductor with a band gap of 3.84 eV [28,29]. Electrons and holes are prevalent in semiconductors and significantly influence their electrical and mechanical properties [30–32]. Our findings reveal that electron injection into B_4C enhances both strength and ductility, affecting the amorphization of B_4C [33]. Conversely, hole injection into B_4C leads to increased strength but reduced ductility [33]. Electron-hole (e-h) pairs also play a crucial role in the behavior of semiconductors. When exposed to light irradiation of an appropriate wavelength, electrons near the valence-band maximum (VBM) become excited to the conduction-band minimum (CBM), resulting in the formation of e-h pairs [34]. These e-h pairs significantly impact the mechanical behaviors of semiconductors, a phenomenon referred to as the photomechanical effect [35–39]. In our recent work, we discovered that excited e-h pairs reduce the ideal shear strength of B_4C without altering the failure mechanism. This reduction occurs due to the redistribution of electrons and holes among the cage and intericosahedral bonds, weakening the B–C bond between adjacent icosahedra [40].

Extensive research has been conducted on the photomechanical effect in covalent/ionic semiconductors [35,37,38]. Dislocation and deformation twinning are two dominant deformation mechanisms in II–VI semiconductors. TEM *in situ* experiments [41,42] revealed that electron-irradiation beams influence dislocation motion in these II–VI ionic semiconductors. Notably, dislocation mobility in ZnS is proportional to the intensity of the electron beam, whereas screw dislocations in CdTe oscillate under electron excitation, eventually forming a zigzag dislocation [41]. The nonradiative recombination of e-h pairs at dislocation cores is responsible for the enhanced dislocation motion [41]. The recombination of e-h pairs has also been found to reduce the activation energy of dislocation nucleation [43]. Furthermore, distinct deformation mechanisms have been observed in cubic ZnS under different light conditions [44]. ZnS exhibits extraordinary plasticity and can sustain deformations of up to 45% strain in complete darkness [44]. Following deformation, the band gap of deformed ZnS decreases by 0.6 eV [44]. In contrast, ZnS subjected to light irradiation during deformation fractures immediately, undergoing brittle failure [44]. This suggests that light exposure can modulate the mechanical strength and fracture toughness in semiconductors.

To gain further insight into this intriguing behavior, constrained density-functional theory (CDFT) simulations were employed to investigate the impact of excited e-h pairs on the mechanical behavior of ZnS [45]. Under light illumination, ZnS tends to exhibit greater twinnability, leading to brittle failure [45]. In addition to II–VI ionic semiconductors, the mechanical behavior of III–V semiconductors is also influenced by e-h pairs [43,46–50]. Prior experimental studies have demonstrated that electronic excitation, such as electron-beam irradiation and laser-light illumination, enhances dislocation mobility in GaAs [46]. Similarly, dislocation mobility is augmented due to a reduction in the apparent activation energy, a phenomenon associated with recombination-enhanced defect reactions [49]. Moreover, nanoindentation experiments, CDFT simulations, and TEM measurements were integrated to examine the photomechanical effects on III–V semiconductors, including InP, GaAs, and GaP [50]. Our findings indicate that light irradiation renders III–V semiconductors more ductile and reduces the energy barrier for deformation slip, which can be attributed to the excited electron-hole pairs (EHPs) weakening covalent bonds.

Distinct from the failure mechanisms of II–VI ionic and III–V covalent semiconductors (dislocations [41] and deformation twinning [45]), B_4C undergoes shear-induced amorphization [20,23,51–53], and the deformation mechanism of nanotwinned B_4C is related to the directional nature of covalent bonds suppressing the twin-boundary slip [13]. However, the effect of electron excitation on nanotwinned B_4C remains unexplored. In this study, we employed CDFT simulations to investigate the influence of e-h pair excitation on the failure mechanism of nanotwinned B_4C. We analyzed the shear deformation of both asymmetric and symmetric twins along the most plausible slip system of TB under the e-h excited state. Compared to the ground state ($0h0e$), the ideal strength of asymmetric twin decreases under e-h excitation, and e-h excitation further increases the brittleness of asymmetric twin. Interestingly, after excitation, the destruction of icosahedra is less severe than that under the $0h0e$ state, suggesting that e-h excitation modifies the deformation mechanism of asymmetric twin. The decreased strength is attributed to the redistribution of excited e-h pairs near TB, with excited electrons surrounding cage B and C atoms connected to neighboring icosahedra, while excited holes preferentially locate in the center of intericosahedral B–C bonds and disperse among the $B_{11}C$ icosahedron. The B–C bonds are weakened by e-h pair excitation, softening nanotwins. Additionally, the reduced ductility phenomenon results from excited EHPs weakening the bonds connecting icosahedral and chain atoms and destabilizing the $B_{11}C$ icosahedra on the upper side of the TB.

Moreover, excited e-h pairs decrease the ideal strength of symmetric twin without affecting the critical shear strain. The findings indicate that e-h excitation significantly weakens the B–C bonds, leading to the decreased strength of nanotwinned B_4C. In contrast to asymmetric twin, the destruction of icosahedra in symmetric twin under the e-h excited state is more severe than that under the $0h0e$ state, implying that excited e-h pair exacerbates the deformation mechanism of symmetric twin. This work provides deeper insight into how excited e-h pairs interact with TBs and further influence the deformation mechanism of nanotwins.

II. COMPUTATIONAL METHODOLOGY

All the simulations in this work were performed using the VASP package, a periodic and plane-wave based code [54–56]. To examine the electronic exchange and correlation energy, the generalized gradient approximation (GGA)-type Perdew-Burke-Ernzerhof functional [57] was applied. The projector

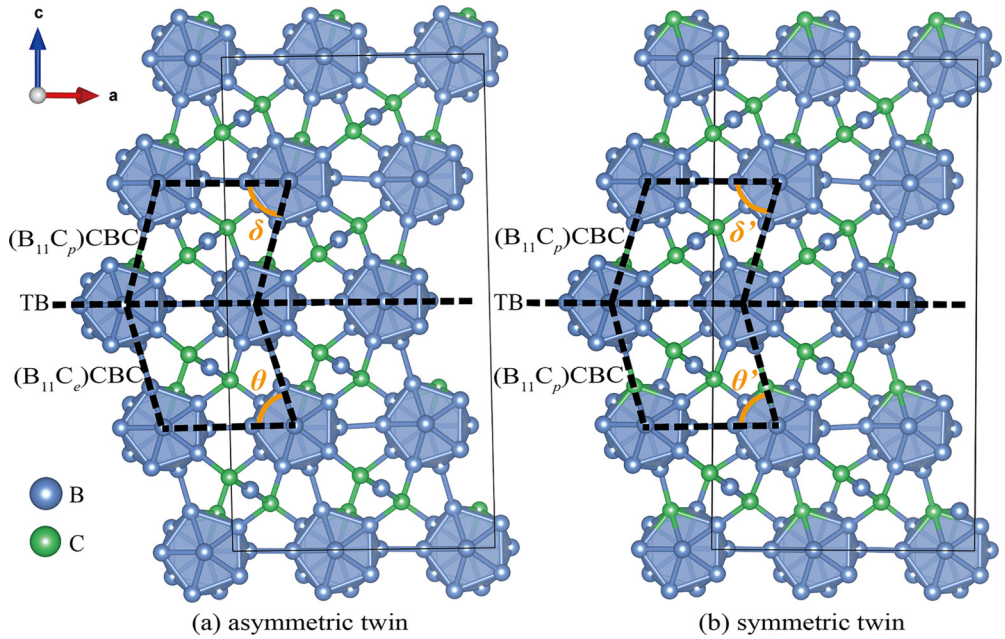

FIG. 1. DFT-predicted nanotwinned B_4C structures. (a) Asymmetric twin with the lowest-energy structure $(B_{11}C_p)$CBC on the upper side of the TB and higher-energy structure $(B_{11}C_e)$CBC on the lower side of the TB; (b) Symmetric twin contains $(B_{11}C_p)$CBC on both sides of the TB.

augmented-wave formalism was used to describe the interaction between ion cores and valence electrons. A 500-eV cutoff energy was used in all DFT simulations. During geometry optimization, the total energy was converged to an accuracy of 10^{-5} eV, and the force convergence on each ion was set as 10^{-3}eV/Å. The tetrahedron method with Blöchl correction [58] was used to calculate the partial occupancy of each orbital. The *K*-point mesh based on the Monkhorst-Pack grid approach was applied to evaluate the Brillouin-zone integration.

We applied the CDFT scheme [56,59–64], where the occupation of the electronic state is fixed to the particular configuration, to characterize the e-h excitation in nanotwinned B_4C. The occupation matrix of excited holes or electrons was obtained by subtracting an electron from or adding an electron to the neutral system. Assuming that small structure change has no appreciable impact on the excited e-h configurations, the electron/hole occupation configuration is fixed during the structure relaxation at each shear strain.

To explore the failure mechanism, we performed the ideal shear deformation on asymmetric and symmetric twins along the twin boundary ((001)[100] slip system in rhombohedral unit cell of B_4C) since previous research established it as the most plausible system for B_4C twin structure [13]. With the exception of the applied shear strain, all of these computations allowed the structure parameters to relax along each of the five strain components [65]. After relaxation, the residual stresses were less than 0.2 GPa. During shear deformation, a $(3 \times 6 \times 1)$ *K*-point grid was employed for both systems (containing 120 atoms). In DFT simulations, the small supercell results in high carrier concentrations of $\sim 1.14 \times 10^{21}$ cm^{-3} for asymmetric twin and $\sim 1.15 \times 10^{21}$ cm^{-3} for symmetric twin, equivalent to the highly doped semiconductors [30–32].

The LOBSTER package was used to perform all crystal orbital Hamilton population (COHP) analyses [66,67]. The COHP, which refers to partitioning the band-structure energy in terms of orbital-pair contributions, can be applied to calculate the nature of the bonding between atoms. In general, the negative, positive, and zero values of COHP(E) suggest the bonding, antibonding, and nonbonding nature.

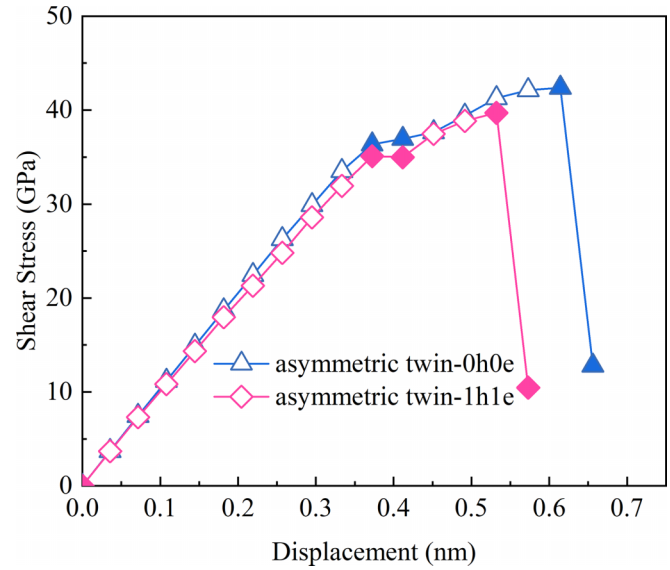

FIG. 2. Relationship of shear stress and displacement of asymmetric twin for the (001)[100] slip system under the ground state $(0h0e)$ and the one e-h pair excited state $(1h1e)$, respectively. Color-filled patterns in the figure represent the key failure steps displayed in subsequent Fig. 3 and Fig. 4.

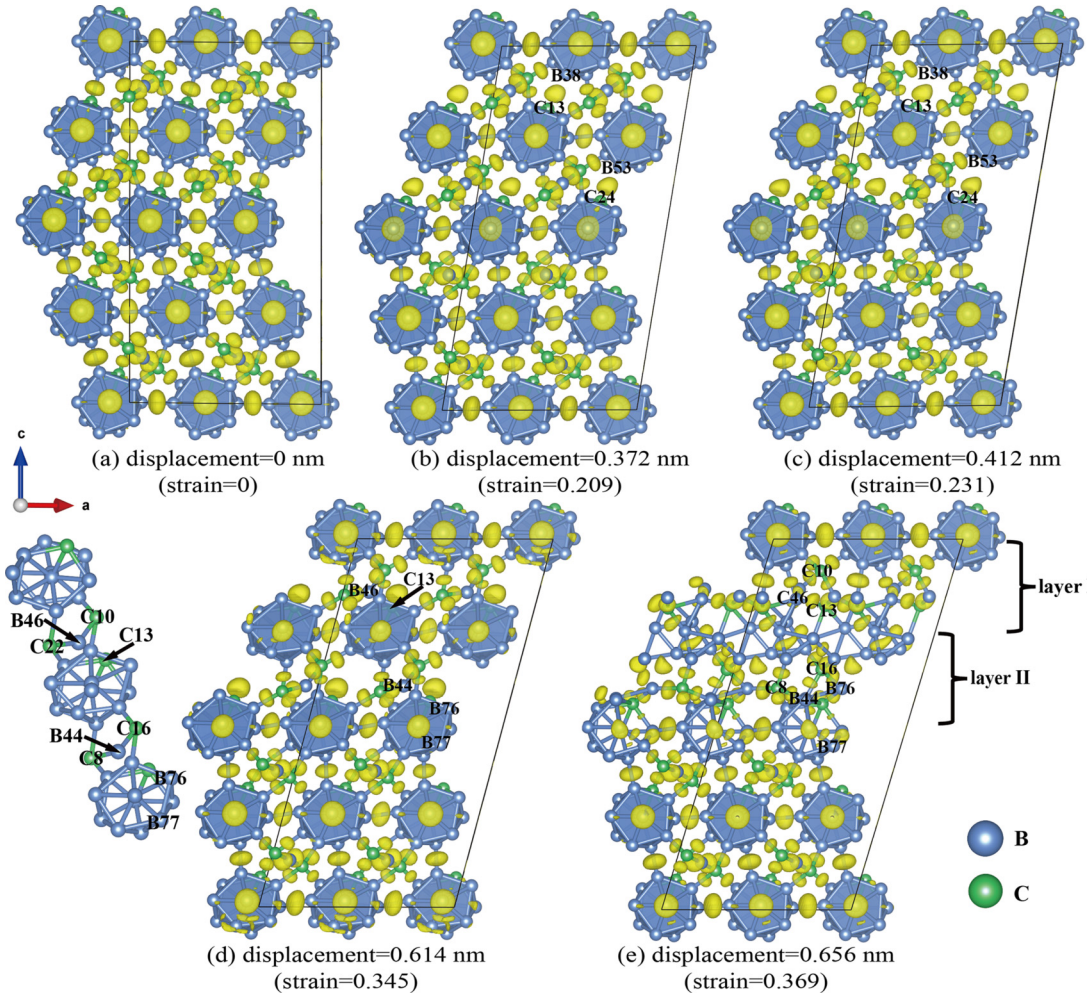

FIG. 3. Structure evolution of asymmetric twin along (001)[100] slip system under the 0h0e state: (a) The intact structure; (b) The structure undergoes elastic deformation when displacement is 0.372 nm (at 0.209 shear strain); (c) Intericosahedral C13–B38 and C24–B53 bonds break as displacement increases to 0.412 nm (at the shear strain of 0.231); (d) C-B-C chains bending at 0.614-nm displacement (the shear strain of 0.345) corresponding to the maximum stress; (e) Complete destruction of icosahedra occurs at 0.656 nm (as well as the shear strain of 0.369). Isosurface value of ELF (represented by yellow isosurface) is 0.85.

Projected COHP (pCOHP) allows the chemical bond to be projected from plane wave. Furthermore, the integrated pCOHP (IpCOHP) is an indicative of the bond strength by integrating the COHP up to the highest-occupied bands. A higher value of IpCOHP indicates greater bond strength [68]. The charge-density difference between the e-h excited state and ground state was calculated to evaluate the distribution of electrons and holes under EHP excitation. During shear deformation, the electron localization function (ELF) [69,70] was employed to probe the bond breaking and rearrangement. VESTA software was employed to display the crystal structure, ELF, and charge-density difference [71].

III. RESULTS AND DISCUSSION

A. Nanotwinned structure in B_4C under e-h excited states

To elucidate the atomic structures of asymmetric twins, we constructed twinned models with (001) planes serving as the TB. As depicted in Fig. 1(a), two layers of ($B_{11}C_p$)CBC structures are on the upper side and two layers of ($B_{11}C_e$)CBC structures are on the lower side. The asymmetric twin model contains 120 atoms. DFT simulations yield the equilibrium lattice parameters: $a = 1.041$ nm, $b = 0.521$ nm, $c = 1.780$ nm, $\alpha = 90.91°$, $\beta = 90.91°$, and $\gamma = 65.00°$. The lattice parameters are changed to $a = 1.041$ nm, $b = 0.521$ nm, $c = 1.782$ nm, $\alpha = 90.90°$, $\beta = 90.90°$, and $\gamma = 65.00°$ under e-h excitation with an e-h concentration of 1.14×10^{21} cm^{-3}. With electron-hole excitation, the cell volume changes from 0.8742 to 0.8744 nm^3, suggesting that electron excitations have minimal impact on the lattice constants. The inclination angles were measured to be $\delta = 74.9°$ and $\theta = 72.8°$, consistent with previous experimental work [13] of $\delta = 74.9°$ and $\theta = 72.3°$.

We constructed a symmetric twinned model with (001) planes as the TB. As illustrated in Fig. 1(b), ($B_{11}C_p$)CBC structures are present on both sides of the TB. This structure contains 120 atoms. DFT simulations provide the equilibrium lattice parameters: $a = 1.042$ nm, $b = 0.521$ nm, $c = 1.773$ nm, $\alpha = 90.00°$, $\beta = 90.00°$, and $\gamma = 65.28°$. Under e-h excited states with concentrations of $\sim 1.15 \times 10^{21}$ cm^{-3}, the

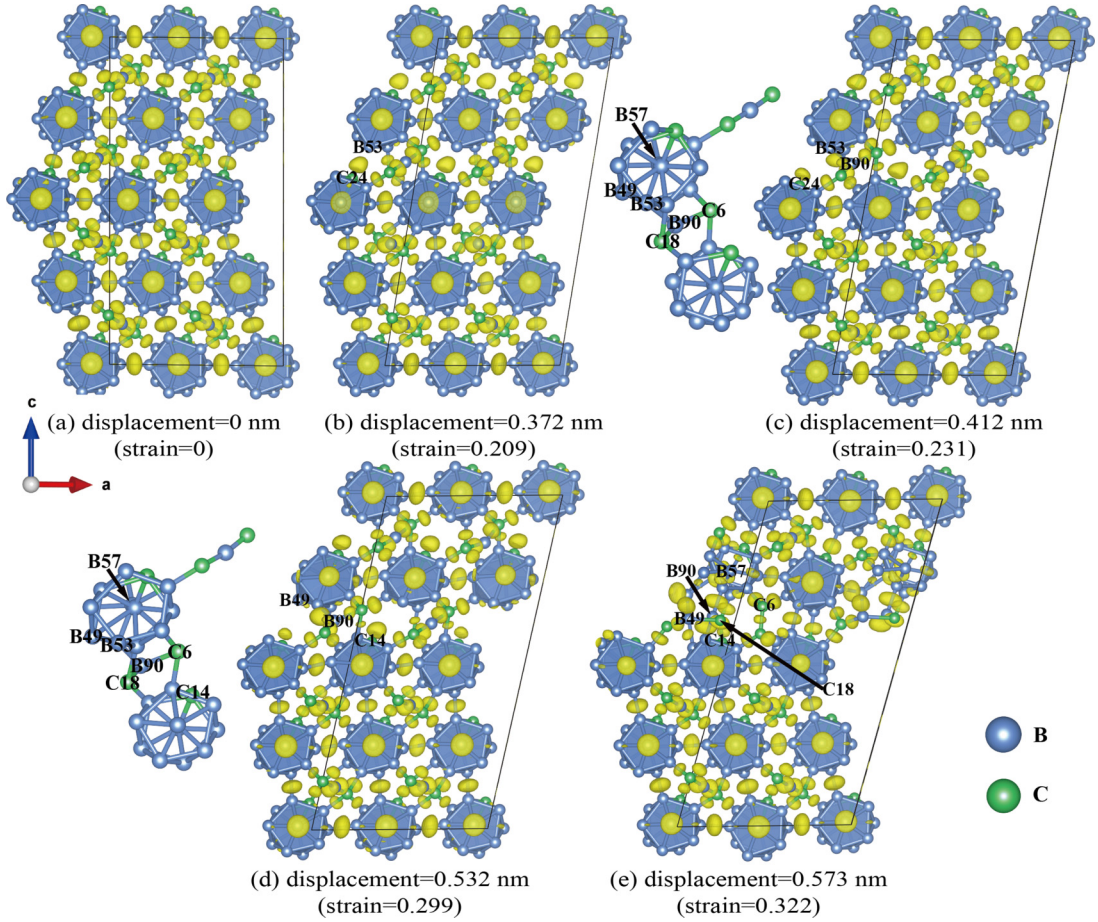

FIG. 4. Structure evolution of asymmetric twin along (001)[100] slip system under the $1h1e$ state: (a) The intact structure; (b) The structure undergoes elastic deformation at 0.372-nm displacement (the shear strain of 0.209); (c) C24–B53 bond breaks and B53 atom reacts with B90 atom at 0.412-nm displacement (0.231 shear strain). (d) When the displacement increases to 0.532 nm (the shear strain increase to 0.299), the shear stress reaches the maximum value. (e) Failure starts by the intraicosahedral B49–B57 bond and the B90–C6 break at 0.573-nm displacement (at 0.322 shear strain). The isosurface value of ELF (represented by yellow isosurface) is 0.85.

lattice constants are changed to $a = 1.041$ nm, $b = 0.521$ nm, $c = 1.774$ nm, $\alpha = 90.90°$, $\beta = 90.90°$, and $\gamma = 65.35°$, suggesting that the e-h excitation has minimal effect on the lattice constants of the symmetric twin. The inclination angles from our predictions were $\delta' = \theta' = 73.8°$, which are in good agreement with the experimental value of $\delta' = 73.1$ and $\theta' = 73.3°$ [13,16].

B. The effect of e-h excitation on asymmetric twin

Our prior research [13] has demonstrated that shearing along the (001) plane, the TB plane, is more favorable compared to the plane perpendicular to the TB. Therefore, we employed the ideal shear deformation along (001)[100] slip system to investigate the failure mechanism of the asymmetric twin under e-h pair excitation with carrier concentrations of $\sim 1.14 \times 10^{21}$ cm^{-3} ($1h-1e$ per supercell).

Figure 2 presents the relationship between shear stress and displacement for the asymmetric twin in the (001)[100] slip system under both the ground state ($0h0e$) and one e-h pair excited state ($1h1e$). The corresponding shear-stress–shear-strain curves are displayed in Fig. S1 of Supplemental Material (SM) [72]. For the asymmetric twin, the ideal shear strength is 39.72 GPa under the $1h1e$ state, which is 8.46% lower than that of the $0h0e$ state (43.39 GPa). Simultaneously, the critical displacement decreases to 0.532 nm (0.299 critical failure strain) with $1h-1e$ compared to 0.614 nm (0.345 critical failure strain) under the $0h0e$ state. Consequently, e-h excitation leads to weakening of both the strength and ductility of the asymmetric twin.

Figure 3 illustrates the shear-induced deformation mechanism of the asymmetric twin along the (001)[100] slip system under $0h0e$ state. Figure 3(a) presents the intact structure being subjected to elastic deformation until the displacement reaches 0.372 nm (the shear strain reaches 0.209) [Fig. 3(b)]. During the elastic deformation, the B53–C24 and B38–C13 bonds connecting adjacent icosahedra on the upper side of the TB are stretched; however, the ELF indicates they are not broken. As displayed in Fig. 3(c), the ELF demonstrates that these two intericosahedral B–C bonds break at 0.412-nm displacement (and at a 0.231 shear strain), resulting in a carbene of lone-pair electrons. Concurrently, the B38–C13 and B53–C24 bond distances, varying with displacement (Fig. S2 of SM [72]), suggest that the distances of these bonds increase continuously until the displacement reaches 0.412 nm (the shear strain reaches 0.231). This is consistent with the ELF

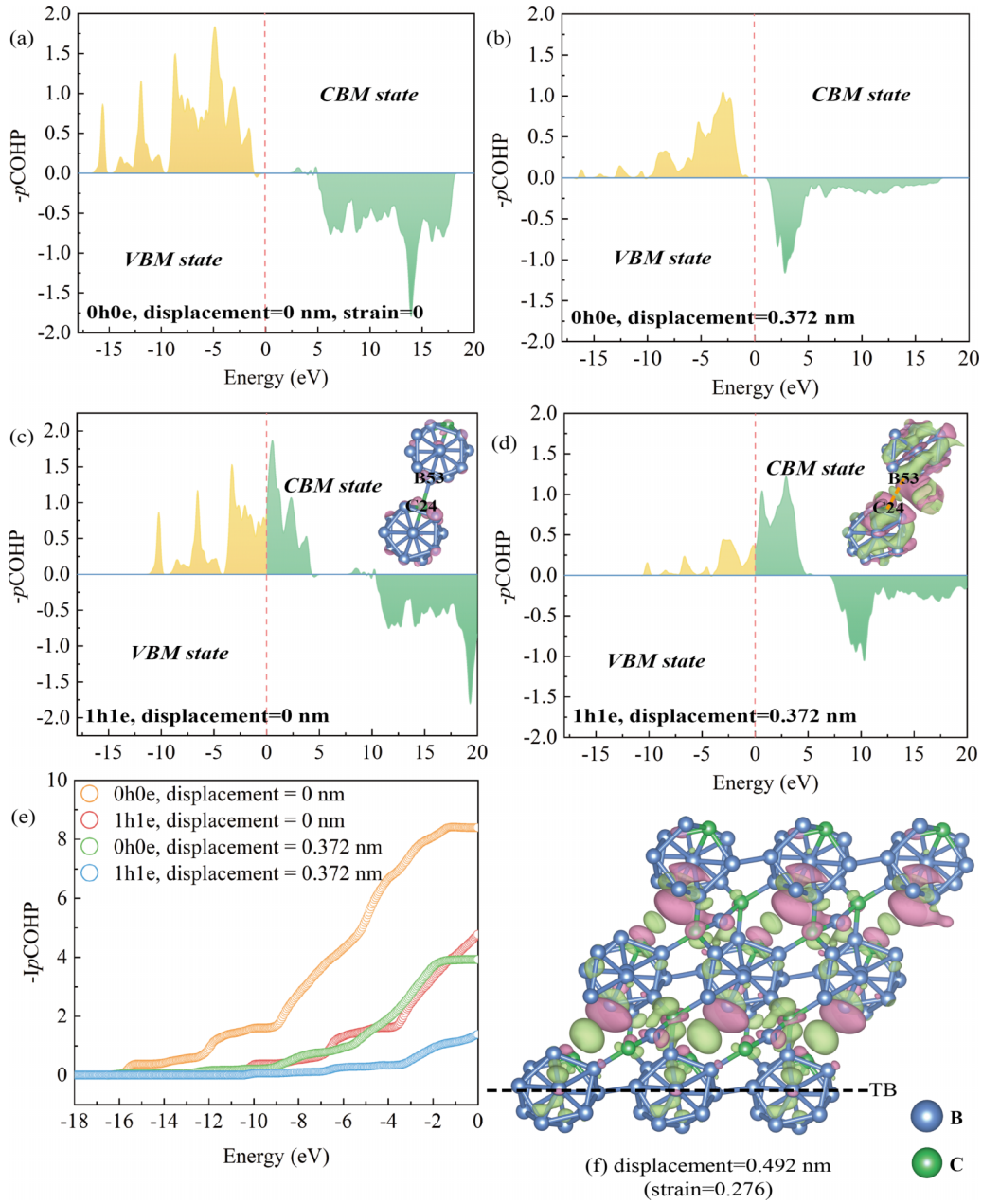

FIG. 5. *p*COHP analysis for the intericosahedral C24–B53 bond under the 0*h*0*e* and 1*h*1*e* states: (a) The intact structure under the 0*h*0*e* state; (b) The deformed structure (displacement = 0.372 nm, shear strain = 0.209) under the 0*h*0*e* state; (c) The intact structure under the 1*h*1*e* state; (d) The deformed structure (displacement = 0.372 nm, shear strain = 0.209) under the 1*h*1*e* state; (e) I*p*COHP for C24–B53 bond; (f) Charge-density difference between the 1*h*1*e* state and the 0*h*0*e* state for the structure before icosahedral fracture (displacement = 0.492 nm, shear strain = 0.276). For the intact and deformed structures, the charge-density difference between the 1*h*1*e* state and 0*h*0*e* state is inserted in (c) and (d), respectively. Light green and light orange represent the electronic orbitals of valence-band maximum (VBM) and conduction-band minimum (CBM), respectively; pink and lime represent the electronic and hole densities caused by e-h excitation, respectively.

analysis, indicating that the B–C bond between adjacent icosahedra breaks as the displacement increases to 0.412 nm (the shear strain increases to 0.231). At a 0.614-nm displacement (0.345 shear strain) [Fig. 3(d)], the shear stress attains its maximum value of 42.39 GPa. On the upper side of the TB, the angles of C22-B46-C10 and C8-B44-C16 chains bend to 143.63° and 155.34°, respectively. The C-B-C chain moves closer to the carbene formed at 0.412 nm displacement (as well as 0.231 shear strain) due to the intericosahedral bonds breaking. In addition, the intraicosahedral B76–B77 bond is stretched. As the displacement increases to 0.656 nm (shear strain further increases to 0.369) [Fig. 3(e)], the failure process exhibits a two-step (layer I and layer II) process on the upper side of the TB: (1) layer I: the central B46 atom in the C22-B46-C10 chain reacts with the carbene C13, leading to the breakage of the B46–C10 bond (the distance increases

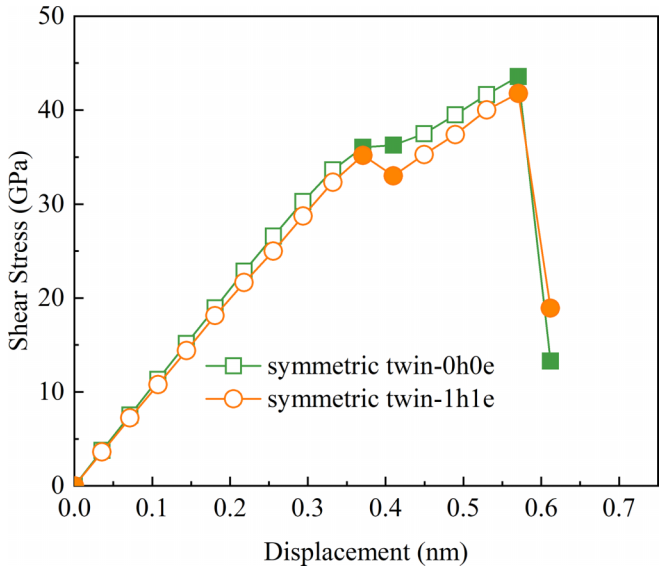

FIG. 6. Relationship of shear stress and displacement of the symmetric twin for the (001)[100] slip system under the ground state ($0h0e$) and the one e-h pair excited state ($1h1e$). The color-filled patterns in the figure represent the key failure steps shown in subsequent Fig. 7 and Fig. 8.

from 0.167 to 0.304 nm) and the complete destruction of the icosahedra; (2) layer II: the B76–B77 bond is stretched from 0.184 to 0.296 nm, and the B76 atom bonds to the C16 atom in the C-B-C chain, destroying the icosahedra.

Under the $1h1e$ state, Fig. 4 depicts the key structural change for the shear-induced deformation mechanism of the asymmetric twin along the (001)[100] slip system. Figure 4(a) illustrates the intact structure of asymmetric twin. In Fig. 4(b), the structure undergoes elastic deformation at 0.372-nm displacement (a 0.209 shear strain). Analogous to the $0h0e$ state, the B53–C24 bond between icosahedra on the upper side of the TB is stretched, while the ELF suggests that this bond is not broken. As exhibited in Fig. S3 of SM [72], the distance of the B53–C24 bond varies with displacement, indicating that it is stretched continuously until the displacement reaches 0.412 nm (at a 0.231 shear strain). In Fig. 4(c), the distance of this B–C bond increases from 0.204 nm (at 0.372-nm displacement (or 0.209 shear strain)) to 0.284 nm (at 0.412-nm displacement (or 0.231 shear strain)), resulting in the bond breaking and cage C forming a lone pair of electrons. Additionally, the B53 atom bonds to the central B90 atom in the C18-B90-C6 chain, and the angle of C18-B90-C6 is bent to 137.24°.

The shear stress reaches its maximum value of 39.71 GPa when the displacement is 0.532 nm (at 0.299 shear strain) [Fig. 4(d)]. The angle of C18-B90-C6 is further bent to 132.76°. The intraicosahedral B49–B57 bond is stretched to 0.242 nm. At 0.573-nm displacement (a shear strain of 0.322) [Fig. 4(e)], the intraicosahedral B49–B57 bond and the B90–C6 bond in the C-B-C chain are stretched to 0.362 and 0.302 nm, respectively, forming bonds between the icosahedral B49 atom and the chain C (C18), and the icosahedral C14 atom and the chain C18 atom. This necessitates the deconstruction of the part above the TB. Notably, only one icosahedron is destroyed in the system, indicating that the failure mechanism of the asymmetric twin is modified by e-h excitation. However, the reduced critical displacement (as well as critical strain) and shear strength suggest that the mechanical properties of asymmetric twins under e-h excitation are compromised.

To gain insights into the physical mechanisms by which e-h excitation affects the deformation behavior of nanotwinned B_4C, we performed *p*COHP analysis to investigate bond strength and bonding information. The -*p*COHP curves were calculated for the intericosahedral B53–C24 bond in four structures: two intact structures (displacement = 0.0 nm, shear strain = 0.0) under $0h0e$ and $1h1e$ states, respectively, and two deformed structures (displacement = 0.372 nm, shear strain = 0.209) under $0h0e$ and $1h1e$ states, as illustrated in Figs. 5(a)–5(d). We also calculated the charge-density difference between the $1h1e$ and $0h0e$ states to show the modified distribution of electron/hole under e-h excitation. In addition, we integrated the -*p*COHP of the B53–C24 bond for both intact and deformed structures to investigate the effect of e-h excitation on bond strength.

Under the $0h0e$ state, both intact and deformed structures exhibit positive -*p*COHP values (i.e., bonding) below the Fermi level (the VBM), and negative -*p*COHP values (i.e., antibonding) above the Fermi level (the CBM), as displayed in Figs. 5(a)–5(b). A band gap is also noticeable between the VBM and CBM. The bonding and antibonding characters for the intact and deformed structures under $1h1e$ state are displayed in Figs. 5(c) and 5(d). With e-h excitation, the Fermi level for both intact and deformed structures shifts from being at the band gap to contacting the bonding state. Figures 5(c) and 5(d) illustrates the charge-density difference for intact/deformed structures between the $1h1e$ and $0h0e$ states. Excess hole states are observed in the cage and in the center of the intericosahedral B–C bond. Conversely, the excess electron states around the B53 and C24 atoms suggest that the transfer of electrons from the cage and the intericosahedral bond to B and C atoms weakens the icosahedra and the intericosahedral bonding, reducing the shear strength. The value of -I*p*COHP [Fig. 5(e)] under the $0h0e$ state is lower than that under the $1h1e$ state, suggesting that excited e-h pairs decrease the intraicosahedral B53–C24 bond strength, which confirms our findings of e-h excitations weakening the B–C bond.

To explain the lower ductility with e-h excitation, we calculate the charge-density difference between the $1h1e$ and $0h0e$ states when the displacement is 0.492 nm (0. 276 shear strain). As illustrated in Fig. 5(f), most excess electron states are concentrated in the boron and carbon atoms connected to the neighboring icosahedra, while a few are distributed around the chain atoms. Conversely, the excess hole states are distributed (1) in the cage; (2) among the bonds that connect the chain and the icosahedra; and (3) among the intericosahedral B–C bonds. These results indicate that e-h excitation weakens two types of bonds: (1) the B–C bond between icosahedra and (2) the bonds between icosahedra and chains, which destabilize the cage and reduce the ductility and strength of nanotwinned B_4C.

C. The effect of e-h excitation on symmetric twin

Next, we investigate the effect of e-h excitation on the failure mechanism of symmetric twin in B_4C. Prior

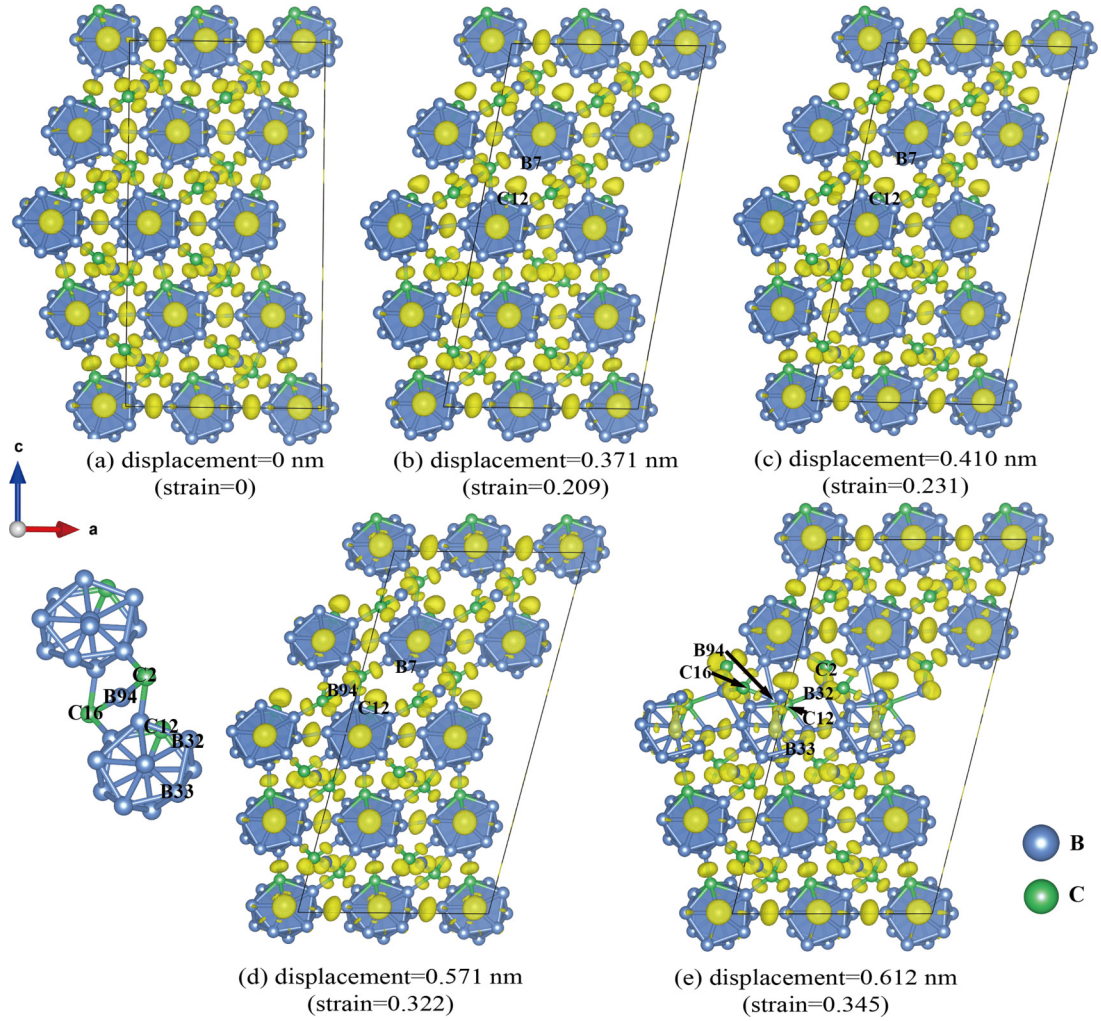

FIG. 7. The symmetric twin evolves along (001)[100] slip system under the 0*h*0*e* state: (a) The intact structure; (b) The structure undergoes elastic deformation at 0.371-nm displacement (as well as 0.209 shear strain); (c) Intericosahedral B7–C12 bond breaks when the displacement increases to 0.410 nm (a 0.231 shear strain); (d) At 0.571-nm displacement (the shear strain of 0.322), the C-B-C chain bends; (e) At 0.612-nm displacement (as well as 0.345 shear strain), the icosahedra at TB are fully destroyed. Value of ELF (represented by yellow isosurface) is 0.85.

theoretical study on nanotwinned B_4C [13] reported that both asymmetric and symmetric twins enhance the strength of the perfect crystal, but symmetric twins increase it more than asymmetric twins. To understand how e-h excitation affects the failure mechanism of symmetric twin, we conducted ideal shear deformation on symmetric twin under the 0*h*0*e* and 1*h*1*e* ($n_i \sim 1.15 \times 10^{21}$ cm^{-3}) states along the (001)[100] slip system. Figure 6 displays the relationship between shear stress and displacement of symmetric twin under these two states. The corresponding shear-stress–shear-strain curves are shown in Fig. S4 of SM [72]. The results show that e-h excitation reduces the ideal shear strength of symmetric twin to 41.78 GPa [critical displacement is 0.571 nm (0.322 critical shear strain)], which is 4.13% lower than that of the 0*h*0*e* state (43.58 GPa). However, excited e-h pairs do not affect the critical displacement (or critical shear strain), indicating that e-h pairs decrease the strength of symmetric twins without compromising their ductility. These findings suggest that e-h excitation plays a crucial role in the failure mechanism of symmetric twin in B_4C and may have significant implications for the design of nanomaterials with enhanced mechanical properties.

Under both 0*h*0*e* and 1*h*1*e* states, the detailed deformation mechanism of symmetric twin along the (001)[100] slip system was examined. Figure 7 displays the evolution of the symmetric twin structure at various important displacements (as well as strains) and the ELF analysis under the 0*h*0*e* state. The initial structure is shown in Fig. 7(a), which undergoes elastic deformation under continuous displacement up to 0.371 nm (shear strain up to 0.209) [Fig. 7(b)]. The ELF analysis reveals that the intericosahedral B7–C12 bond remains intact. As the displacement further increases to 0.410 nm (the shear strain further increases to 0.231) [Fig. 7(c)], the ELF of B7–C12 bond shifts entirely to the cage C12 atom, suggesting that this bond is broken. This is also confirmed by the change in the distance of the B–C bond with displacement, as shown in Fig. S5 of SM [72]. At 0.571-nm displacement (0.322 shear strain) [Fig. 7(d)], the shear stress reaches its maximum value, and the three-atom chain C16-B94-C2 bends to 169.57°. As the displacement (as well as shear strain)

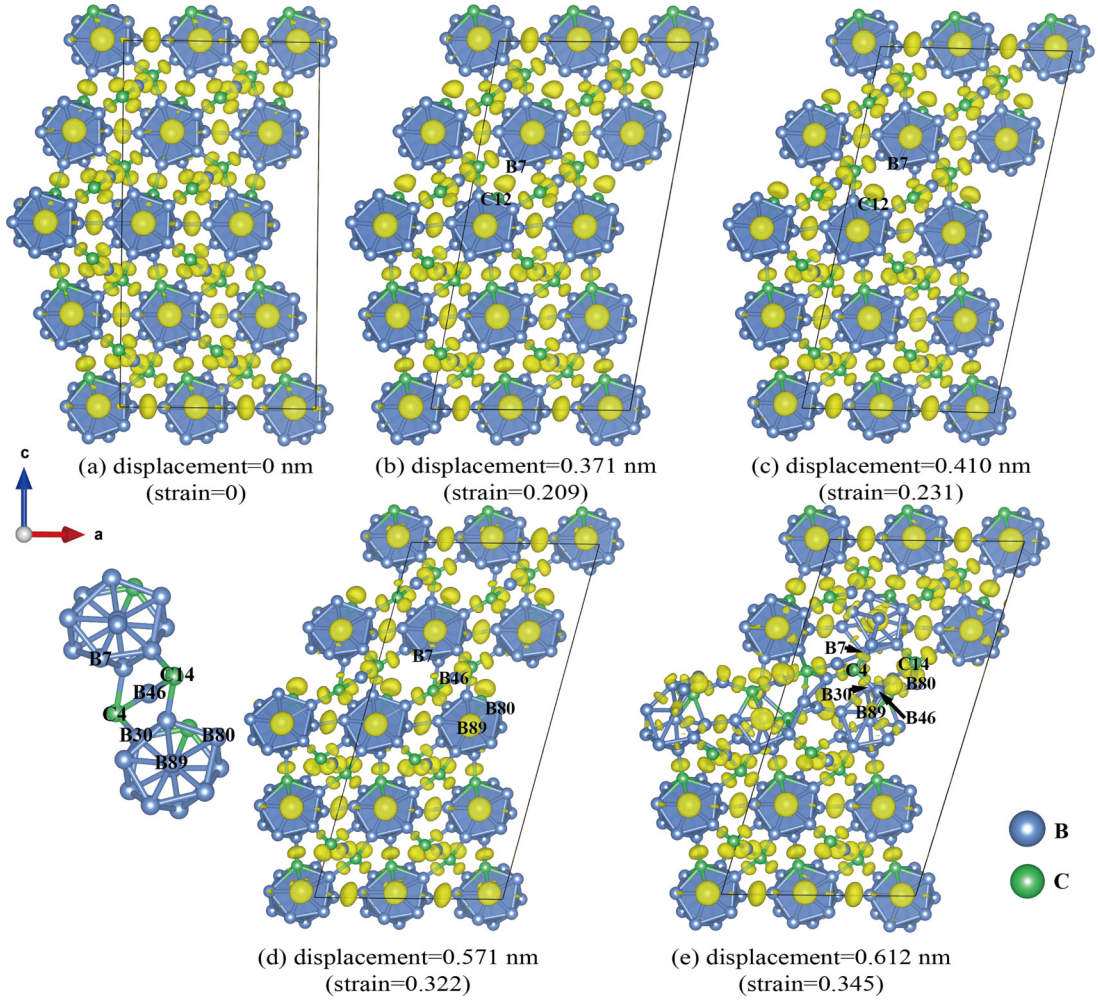

FIG. 8. The symmetric twin evolves along (001)[100] slip system under 1*h*1*e* state: (a) The intact structure; (b) At 0.371-nm displacement (as well as 0.209 shear strain), the structure undergoes elastic deformation; (c) The intericosahedral B7–C12 bond is broken at a displacement of 0.410 nm (0.231 shear strain); (d) At 0.571-nm displacement (0.322 shear strain), the C-B-C chain bent; (e) At a displacement of 0.612 nm (0.345 shear strain), the icosahedra are destroyed. Value of ELF (represented by yellow isosurface) is 0.85.

continues to increase, the three-atom chain progressively bends, and the central B94 atom moves closer to the icosahedral C12 atom. In Fig. 7(e), B94 interacts with C12 at 0.612-nm displacement (0.345 shear strain), forming a new B94–C12 bond. In addition, the B94–C2 bond is drastically stretched from 0.156 to 0.306 nm, indicating that this bond is broken. Simultaneously, the distance of the intraicosahedral B32–B33 bond increases from 0.184 to 0.326 nm, forming a new B32–C2 bond. This results in the fracture of the icosahedra at TB.

For symmetric twin under the 1*h*1*e* state, Fig. 8 presents the ELF analysis of the structures at crucial displacements (as well as strains). As the shear strain is incrementally applied, the intact structure [Fig. 8(a)] undergoes elastic deformation until the displacement reaches 0.371 nm (the shear strain reaches 0.209). The ELF in Fig. 8(b) reveals that the intericosahedral B7–C12 bond above the TB remains intact at a displacement of 0.371 nm (a shear strain of 0.209). In Fig. 8(c), this bond then breaks at a 0.410-nm displacement (0.231 shear strain), causing the shear stress to decline from 35.18 to 33.00 GPa. The ELF analysis confirms the breaking of that B–C bond, and the change in bond length with displacement (Fig. S6 of SM [72]) further substantiates this bond rupture. At a 0.571-nm displacement (0.322 shear strain), the intraicosahedral B80–B89 bond at TB stretches to 0.210 nm. The angle of the three-atom C4-B46-C14 chain bends to 164.72°. Subsequently, at 0.612-nm displacement (as well as 0.345 shear strain), the B46 atom interacts with the icosahedral B89 atom, as shown in Fig. 8(e). The distance of the B46–C14 bond increases from 0.156 to 0.325 nm. Simultaneously, the intraicosahedral B80–B89 bond stretches to 0.340 nm, resulting in the disintegration of the $B_{11}C$ icosahedra at TB. In addition, the B7 atom in the icosahedra on the upper side of TB interacts with the icosahedral B30 atom, leading to the fracture of the icosahedra on the upper side of TB.

These findings suggest that the breaking of both three-atom C-B-C chain and the intericosahedral B–C bond initiates the structural failure of the symmetric twin under both 0*h*0*e* and 1*h*1*e* states. Besides, unlike asymmetric twin, the number of destroyed icosahedra of symmetric twin under e-h excitation is greater than that under the ground state. This

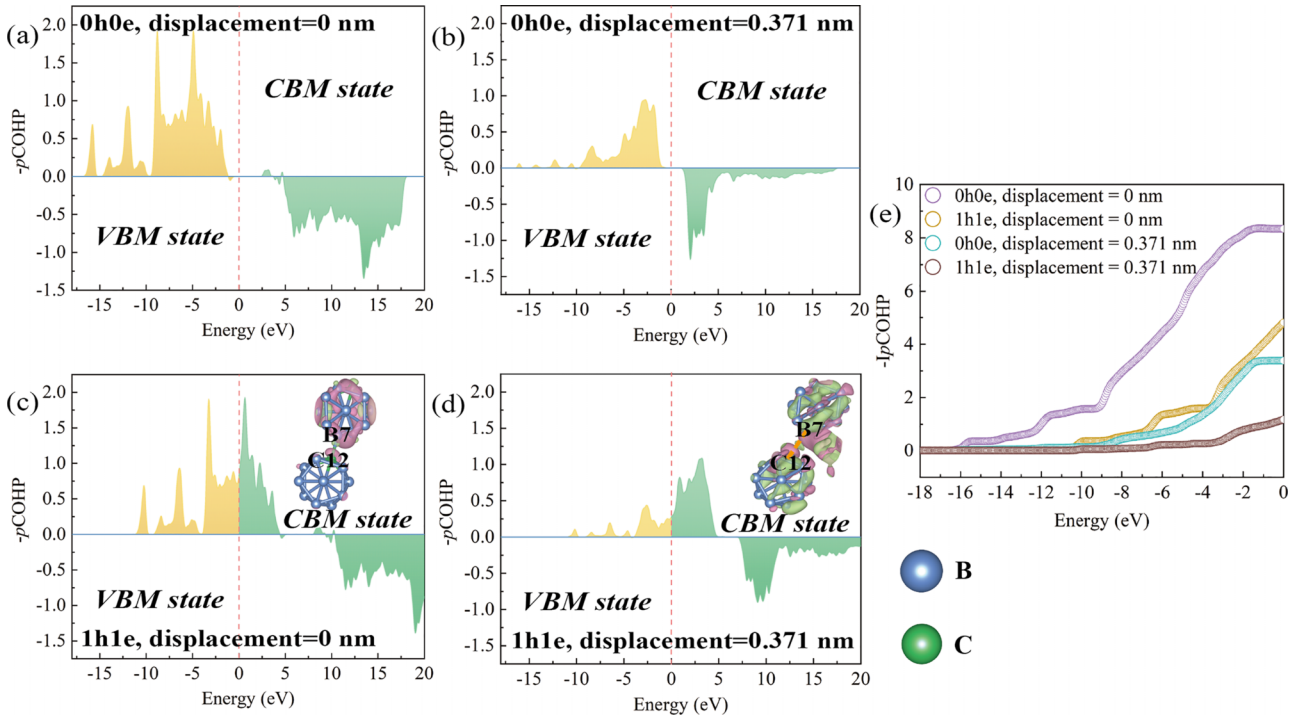

FIG. 9. *p*COHP analysis for the intericosahedral B7–C12 bond under 0*h*0*e* and 1*h*1*e* states: (a) the intact structure at 0-nm displacement (ground state); (b) the deformed structure at 0.371-nm displacement (ground state); (c) the intact structure at 0-nm displacement (excited state); and (d) the deformed structure at 0.371-nm displacement (excited state); (e) I*p*COHP for intericosahedral B7–C12 bond. For the intact and deformed structures, the charge-density difference between the 1*h*1*e* state and 0*h*0*e* state is inserted in (c) and (d), respectively. Light green and light orange represent the electronic orbitals of VBM and CBM, respectively; pink and lime represent the electronic and hole densities caused by e-h excitation, respectively.

observation indicates that e-h excitation exacerbates the deformation mechanism of symmetric twins.

The *p*COHP analysis was employed to explore the underlying cause of the decreased strength in e-h excitation for symmetric twins. We focused on the *p*COHP calculations of B7–C12 bond, as this bond is the first to break under shear deformation, ultimately leading to failure. As depicted in Fig. 9, -*p*COHP curves for the B7–C12 bond under the 0*h*0*e* state and the 1*h*1*e* state are obtained for both the intact (displacement = 0.0 nm, shear strain = 0.0) and deformed (displacement = 0.371 nm, shear strain = 0.209) structures. As demonstrated in Figs. 9(a) and 9(b), the VBM and CBM of the B7–C12 bond consist of bonding and antibonding states under 0*h*0*e* state for both intact and deformed structures. Upon e-h excitation, the Fermi level, which was initially in the band gap, touches the bonding states of both intact and deformed structures, as illustrated in Figs. 9(c) and 9(d).

Furthermore, for both intact and deformed structures, the integrated -*p*COHP (-I*p*COHP) of the B7–C12 bond under the 1*h*1*e* state is lower than that under the 0*h*0*e* state, as shown in Fig. 9(e). This bond weakening can be attributed to the excited e-h pairs, resulting in a decrease in the ideal shear strength under the 1*h*1*e* state. To confirm this, the charge-density difference [Figs. 9(c)–9(d)] between the 1*h*1*e* and 0*h*0*e* states for both intact and deformed structures was calculated. The additional electron state is distributed around the B7 and C12 atoms connecting adjacent icosahedra, while the hole state is (1) dispersed among the cage and (2) located in the center of the intericosahedral B7–C12 bond. This observation suggests that electron transfers from the cage and the intericosahedral bond to the B and C atoms, thereby weakening the icosahedra and the intericosahedral bond, ultimately leading to a reduction in the shear strength.

IV. CONCLUSION

In this work, we employ constrained DFT simulations to investigate the effects of e-h excitations on nanotwinned B_4C, specifically asymmetric and symmetric twins. Our results demonstrate that excited e-h pairs interact with chain and icosahedral atoms near TBs, influencing the deformation mechanisms of nanotwins. Notably, e-h excitations reduce both the ideal shear strength and critical displacement (or critical shear strain) of the asymmetric twin and the ideal shear strength of the symmetric twin. The excited e-h pairs are found to weaken the B–C bond between neighboring icosahedra, leading to a reduction in ideal shear strength. For the asymmetric twin, structural failure is initiated by the breaking of the intericosahedral B–C bond on the upper side of the TB. With $1h-1e$, the excited electrons are distributed around the B and C atoms connecting the neighboring icosahedra, while the excited holes preferentially locate near the intraicosahedral B–B bonds and intericosahedral B–C bonds. This indicates that excited e-h pairs weaken the B–C bonds, thereby reducing the ideal strength of the asymmetric twin. Additionally, the reduction in critical displacement (or critical shear strain) for the asymmetric twin is due to excess holes distributed among the bonds between icosahedra and chains,

destabilizing the cage. Interestingly, however, we find that the number of deconstructed icosahedra under the $1h1e$ state is lower than that of the $0h0e$ state, suggesting that e-h excitation modifies the failure mechanism of the asymmetric twin. The failure mechanism of the symmetric twin can be attributed to the breaking of the intericosahedral B–C bond. Under the $1h1e$ state, this bond is weakened by the redistribution of electrons and holes near TBs. Consequently, the ideal strengths of the symmetric twin under the excited state are lower than those of the ground state. Furthermore, our results reveal that e-h excitation exacerbates the deformation mechanism of the symmetric twin, in contrary to the asymmetric twin. Overall, our study provides atomistic insights into how the excited e-h pairs interact with the TBs of nanotwinned B_4C.

ACKNOWLEDGMENT

Y.S. and Q.A. were supported by the Startup Research Fund from Iowa State University.

[1] Q. Yu, L. Qi, K. Chen, R. K. Mishra, J. Li, and A. M. Minor, The nanostructured origin of deformation twinning, Nano. Lett. **12**, 887 (2012).

[2] K. Lu, L. Lu, and S. Suresh, Strengthening materials by engineering coherent internal boundaries at the nanoscale, Science **324**, 349 (2009).

[3] R. F. Zhang, A. S. Argon, and S. Veprek, Understanding why the thinnest SiN_x interface in transition-metal nitrides is stronger than the ideal bulk crystal, Phys. Rev. B **81**, 245418 (2010).

[4] A. Nie, L.-Y. Gan, Y. Cheng, Q. Li, Y. Yuan, F. Mashayek, H. Wang, R. Klie, U. Schwingenschlogl, and R. Shahbazian-Yassar, Twin boundary-assisted lithium ion transport, Nano. Lett. **15**, 610 (2015).

[5] L. Lu, X. Chen, X. Huang, and K. Lu, Revealing the maximum strength in nanotwinned copper, Science **323**, 607 (2009).

[6] K.-C. Kim, J. Lee, B. K. Kim, W. Y. Choi, H. J. Chang, S. O. Won, B. Kwon, S. K. Kim, D.-B. Hyun, H. J. Kim, H. C. Koo, J.-H. Choi, D.-I. Kim, J.-S. Kim, and S.-H. Baek, Free-electron creation at the 60 ° twin boundary in Bi_2Te_3, Nat. Commun. **7**, 12449 (2016).

[7] J. S. Stolken and A. G. Evans, A microbend test method for measuring the plasticity length scale, Acta. Mater. **46**, 5109 (1998).

[8] Q. An, K. M. Reddy, J. Qian, K. J. Hemker, M.-W. Chen, and W. A. Goddard III, Nucleation of amorphous shear bands at nanotwins in boron suboxide, Nat. Commun. **7**, 11001 (2016).

[9] K. S. Kumar, H. Van Swygenhoven, and S. Suresh, Mechanical behavior of nanocrystalline metals and alloys, Acta. Mater. **51**, 5743 (2003).

[10] B. Li, H. Sun, and C. F. Chen, Large indentation strain stiffening in nanotwinned cubic boron nitride, Nat. Commun. **5**, 4965 (2014).

[11] Y. Tian, B. Xu, D. Yu, Y. Ma, Y. Wang, Y. Jiang, W. Hu, C. Tang, Y. Gao, K. Luo, Z. Zhao, L.-M. Wang, B. Wen, J. He, and Z. Liu, Ultrahard nanotwinned cubic boron nitride, Nature (London) **493**, 385 (2013).

[12] Q. Huang, D. Yu, B. Xu, W. Hu, Y. Ma, Y. Wang, Z. Zhao, B. Wen, J. He, Z. Liu, and Y. Tian, Nanotwinned diamond with unprecedented hardness and stability, Nature (London) **510**, 250 (2014).

[13] Q. An, W. A. Goddard, III, K. Y. Xie, G. D. Sim, K. J. Hemker, T. Munhollon, M. F. Toksoy, and R. A. Haber, Superstrength through nanotwinning, Nano. Lett. **16**, 7573 (2016).

[14] C. Cheng, K. M. Reddy, A. Hirata, T. Fujita, and M. Chen, Structure and mechanical properties of boron-rich boron carbides, J. Eur. Ceram. Soc. **37**, 4514 (2017).

[15] T. Fujita, P. Guan, K. Madhav Reddy, A. Hirata, J. Guo, and M. Chen, Asymmetric twins in rhombohedral boron carbide, Appl. Phys. Lett. **104**, 021907 (2014).

[16] K. Y. Xie, Q. An, M. F. Toksoy, J. W. McCauley, R. A. Haber, W. A. Goddard, and K. J. Hemker, Atomic-Level Understanding of "Asymmetric Twins" in Boron Carbide, Phys. Rev. Lett. **115**, 175501 (2015).

[17] X. Yang, W. A. Goddard III, and Q. An, Asymmetric twins in boron rich boron carbide, Phys. Chem. Chem. Phys. **20**, 13340 (2018).

[18] E. M. Heian, S. K. Khalsa, J. W. Lee, Z. A. Munir, T. Yamamoto, and M. Ohyanagi, Synthesis of dense, high-defect-concentration B_4C through mechanical activation and field-assisted combustion, J. Am. Ceram. Soc. **87**, 779 (2004).

[19] M. W. Chen, J. W. McCauley, J. C. LaSalvla, and K. J. Hemker, Microstructural characterization of commercial hot-pressed boron carbide ceramics, J. Am. Ceram. Soc. **88**, 1935 (2005).

[20] V. Domnich, S. Reynaud, R. A. Haber, and M. Chhowalla, Boron carbide: Structure, properties, and stability under stress, J. Am. Ceram. Soc. **94**, 3605 (2011).

[21] A. O. Sezer and J. I. Brand, Chemical vapor deposition of boron carbide, Mater. Sci. Eng., B **79**, 191 (2001).

[22] F. Thevenot, Boron carbide—a comprehensive review, J. Eur. Ceram. Soc. **6**, 205 (1990).

[23] Q. An, W. A. Goddard, III, and T. Cheng, Atomistic Explanation of Shear-Induced Amorphous Band Formation in Boron Carbide, Phys. Rev. Lett. **113**, 095501 (2014).

[24] Q. An and W. A. Goddard, III, Nanotwins soften boron-rich boron carbide ($B_{13}C_2$), Appl. Phys. Lett. **110**, 111902 (2017).

[25] C. Kunka, X. Yang, Q. An, and G. Subhash, Icosahedral superstrength at the nanoscale, Phys. Rev. Mater. **2**, 063606 (2018).

[26] Y. He, Y. Shen, B. Tang, and Q. An, Strengthening boron carbide through lithium dopant, J. Am. Ceram. Soc. **103**, 2012 (2020).

[27] X. Huang, Y. Shen, and Q. An, Nanotwinning induced decreased lattice thermal conductivity of high temperature thermoelectric boron subphosphide ($B_{12}P_2$) from deep learning potential simulations, Energy and AI **8**, 100135 (2022).

[28] J. Lagrenaudie, A study of the properties of boron, J. Phys. Radium **14**, 14 (1953).

[29] H. Wang and Q. An, Band-gap engineering in high-temperature boron-rich icosahedral compounds, J. Phys. Chem. C **123**, 12505 (2019).

[30] R. W. Miles, G. Zoppi, and I. Forbes, Inorganic photovoltaic cells, Mater. Today **10**, 20 (2007).

[31] P. P. Altermatt, A. Schenk, F. Geelhaar, and G. Heiser, Reassessment of the intrinsic carrier density in crystalline silicon in view of band-gap narrowing, J. Appl. Phys. **93**, 1598 (2003).
[32] A. Kanevce, M. O. Reese, T. Barnes, S. Jensen, and W. Metzger, The roles of carrier concentration and interface, bulk, and grain-boundary recombination for 25% efficient CdTe solar cells, J. Appl. Phys. **121**, 214506 (2017).
[33] Y. He, Y. Shen, B. Tang, and Q. An, Enhanced strength and ductility of superhard boron carbide through injecting electrons, J. Eur. Ceram. Soc. **40**, 4428 (2020).
[34] W. Lambrecht, Dopants and defects in semiconductors, Mater. Today **7**, 349 (2012).
[35] R. E. Hanneman and P. J. Jorgensen, On the existence of electromechanical and photomechanical effects in semiconductors. J. Appl. Phys. **38**, 4099 (1967).
[36] K. Maeda and S. Takeuchi, in *Dislocations in Solids*, edited by F. R. N. Nabarro and M. S. Duesbery (Elsevier, New York 1996), Vol. 10, pp. 443–504.
[37] L. Carlsson and C. N. Ahlquist, Photoplastic behavior of CdTe, J. Appl. Phys. **43**, 2529 (1972).
[38] L. Carlsson and C. Svensson, Photoplastic effect in ZnO, J. Appl. Phys. **41**, 1652 (1970).
[39] S. K. Choi, M. Mihara, and T. Ninomiya, Dislocation velocities in GaAs, Jpn. J. Appl. Phys. **16**, 737 (1977).
[40] Y. He, Y. Shen, B. Tang, and Q. An, Electron–hole excitation induced softening in boron carbide-based superhard materials, ACS Appl. Mater. Interfaces **14**, 25792 (2022).
[41] C. Levade, J. J. Couderc, G. Vanderschaeve, D. Caillard, and A. Couret, TEM insitu observation of recombination-enhanced mobility of dislocations in II-VI compounds, Appl. Surf. Sci. **50**, 119 (1991).
[42] C. Levade and G. Vanderschaeve, Electron-irradiation enhanced dislocation glide in II-VI semiconductors, J. Cryst. Growth **197**, 565 (1999).
[43] M. Werner, M. Bartsch, U. Messerschmidt, and D. Baither, TEM observations of dislocation motion in polycrystalline silicon during in situ straining in the high voltage electron microscope, Phys. Status Solidi **146**, 133 (1994).
[44] Y. Oshima, A. Nakamura, and K. Matsunaga, Extraordinary plasticity of an inorganic semiconductor in darkness, Science **360**, 772 (2018).
[45] H. Wang, S. I. Morozov, W. A. Goddard, III, and Q. An, Light irradiation induced brittle-to-ductile and ductile-to-brittle transition in inorganic semiconductors, Phys. Rev. B **99**, 161202(R) (2019).
[46] K. Maeda, K. Suzuki, M. Ichihara, and S. Takeuchi, Electron-beam irradiation enhanced dislocation glide in GaAs observed by transmission electron microscopy, J. Appl. Phys. **56**, 554 (1984).
[47] P. G. Callahan, B. B. Haidet, D. Jung, G. G. E. Seward, and K. Mukherjee, Direct observation of recombination-enhanced dislocation glide in heteroepitaxial GaAs on silicon, Phys. Rev. Mater. **2**, 081601(R) (2018).
[48] K. Maeda and S. Takeuchi, Enhanced glide of dislocations in GaAs single crystals by electron beam irradiation, Jpn. J. Appl. Phys. **20**, L165 (1981).
[49] K. Maeda and S. Takeuchi, Recombination enhanced dislocation glide in InP single crystals, Appl. Phys. Lett. **42**, 664 (1983).
[50] H. Wang, S. Song, X. Zou, F. Wang, Z. Zhang, S. I. Morozov, X. Wang, K. M. Reddy, and Q. An, Photomechanical effect leading to extraordinary ductility in covalent semiconductors, Phys. Rev. B **100**, 094110 (2019).
[51] R. B. Kaner, J. J. Gilman, and S. H. Tolbert, Designing superhard materials, Science **308**, 1268 (2005).
[52] M. Chen, J. W. McCauley, and K. J. Hemker, Shock-induced localized amorphization in boron carbide, Science **299**, 1563 (2003).
[53] K. M. Reddy, P. Liu, A. Hirata, T. Fujita, and M. W. Chen, Atomic structure of amorphous shear bands in boron carbide, Nat. Commun. **4**, 2483 (2013).
[54] G. Kresse and J. Furthmuller, Efficient iterative schemes for ab initio total-energy calculations using a plane-wave basis set, Phys. Rev. B **54**, 11169 (1996).
[55] G. Kresse and J. Furthmuller, Efficiency of ab-initio total energy calculations for metals and semiconductors using a plane-wave basis set, Comput. Mater. Sci. **6**, 15 (1996).
[56] G. Kresse and J. Hafner, Ab initio molecular dynamics for liquid metals, Phys. Rev. B **47**, 558 (1993).
[57] J. P. Perdew, K. Burke, and M. Ernzerhof, Generalized Gradient Approximation Made Simple, Phys. Rev. Lett. **78**, 1396 (1997).
[58] P. E. Blochl, O. Jepsen, and O. K. Andersen, Improved tetrahedron method for Brillouin-zone integrations, Phys. Rev. B **49**, 16223 (1994).
[59] P. E. Blöchl, Projector augmented-wave method, Phys. Rev. B **50**, 17953 (1994).
[60] B. Kaduk, T. Kowalczyk, and T. Van Voorhis, Constrained density functional theory, Chem. Rev. **112**, 321 (2012).
[61] D. Kidd, A. S. Umar, and K. Varga, Constrained density functional theory calculation with iterative optimization, Phys. Rev. B **98**, 075108 (2018).
[62] G. Kresse and D. Joubert, From ultrasoft pseudopotentials to the projector augmented-wave method, Phys. Rev. B **59**, 1758 (1999).
[63] M. Melander, E. Ö. Jónsson, J. J. Mortensen, T. Vegge, and J. M. García Lastra, Implementation of constrained DFT for computing charge transfer rates within the projector augmented wave method, J. Chem. Theory Comput. **12**, 5367 (2016).
[64] J. P. Perdew, K. Burke, and M. Ernzerhof, Generalized Gradient Approximation Made Simple, Phys. Rev. Lett. **77**, 3865 (1996).
[65] D. Roundy, C. R. Krenn, M. L. Cohen, and J. W. Morris, Ideal Shear Strengths of fcc Aluminum and Copper, Phys. Rev. Lett. **82**, 2713 (1999).
[66] S. Maintz, V. L. Deringer, A. L. Tchougréeff, and R. Dronskowski, LOBSTER: A tool to extract chemical bonding from plane-wave based DFT, J. Comput. Chem. **37**, 1030 (2016).
[67] V. L. Deringer, A. L. Tchougréeff, and R. Dronskowski, Crystal orbital Hamilton population (COHP) analysis as projected from plane-wave basis sets, J. Phys. Chem. A. **115**, 5461 (2011).
[68] S. Steinberg and R. Dronskowski, The crystal orbital Hamilton population (COHP) method as a tool to visualize and analyze chemical bonding in intermetallic compounds, cryst. **8**, 225 (2018).

[69] A. D. Becke and K. E. Edgecombe, A simple measure of electron localization in atomic and molecular systems, J. Chem. Phys. **92**, 5397 (1990).

[70] B. Silvi and A. Savin, Classification of chemical-bonds based on topological analysis of electron localization functions, Nature (London) **371**, 683 (1994).

[71] K. Momma and F. Izumi, VESTA 3 for three-dimensional visualization of crystal, volumetric and morphology data, J. Appl. Crystallogr. **44**, 1272 (2011).

[72] See Supplemental Material at http://link.aps.org/supplemental/10.1103/PhysRevB.107.224102 for the relationship of shear stress and shear strain of asymmetric twin for the (001)[100] slip system under the ground state ($0h0e$) and the one e-h pair excited state ($1h1e$), respectively (Fig. S1); the bond distance of (a) B38–C13 and (b) B53–C24 in asymmetric twin varying with displacement under $0h0e$ state (ground state) (Fig. S2); the bond distance of B53–C24 in asymmetric twin varying with displacement under $1h1e$ state (excited state) (Fig. S3); the relationship of shear stress and shear strain of the symmetric twin for the (001)[100] slip system under the ground state ($0h0e$) and the one e-h pair excited state ($1h1e$), respectively (Fig. S4); the bond distance of B7–C12 in symmetric twin varying with displacement under $0h0e$ state (ground state) (Fig. S5); the bond distance of B7–C12 in symmetric twin varying with displacement under $1h1e$ state (excited state) (Fig. S6).